Optimization of Imperfection-Insensitive Continuous Tow Sheared Rocket Launch Structures

Reece L. Lincoln *, Paul M. Weaver †, Alberto Pirrera ‡, and Rainer M.J. Groh §
Bristol Composites Institute, University of Bristol, UK

Geometric imperfection sensitivity is the largest influencing factor that limits the design of thin-walled monocoque cylinders. Current generation cylindrical architectures, such as those found in rocket launch vehicles, rely on the use of sandwich or blade-stiffened structures to reduce the imperfection sensitivity of the cylinder. Whilst much research has focused on the creation of new knockdown factors that relate to the modern architectures used, this paper focuses on reducing the imperfection sensitivity of a monocoque cylinder from a design perspective. Variable-angle composites that steer the fibers in curvilinear paths offer an opportunity to design structural load paths. By steering the fibers, the effective area over which geometric imperfections influence the buckling behavior of the cylinder is reduced. This diminishes the imperfection sensitivity of thin-walled cylinders undergoing axial compression. Continuous Tow Shearing (CTS) is one such variable-angle manufacturing technique. It does not cause common in-process manufacturing defects associated with Automated Fiber Placement, such as fiber wrinkling or fiber buckling. In addition, there is a shearing angle-thickness coupling that results in local thickness build-ups, which, whilst potentially increasing the mass of the structure, enable embedded stiffeners to be created by shearing the tows. Three genetic algorithm (GA) optimizations are carried out to maximize the imperfect mass-specific buckling load to investigate the efficacy of CTS and tow-steered designs in reducing imperfection sensitivity. The first optimization considers idealistic manufacturing capabilities with a random geometric imperfection. The second and third optimizations consider current manufacturing capabilities and are compared against one another to analyze the use of a evolutionary hybrid GA and a probabilistic, reliability-based GA. In all three optimizations, the optimum laminate from the GA demonstrates imperfection insensitivity.

I. Nomenclature

A_{kl}, B_{kl}	=	Fourier coefficients
E	=	axial stiffness
k, l	=	axial and circumferential wave numbers, respectively
L	=	length of cylinder
M	=	mass of cylinder
n	=	periodicity
$n_1,\ n_2$	=	maximum number of axial and circumferential wave numbers, respectively
N	=	number of layers in laminate
P	=	buckling load
r	=	radius of cylinder
t	=	total laminate thickness
t_0	=	nominal lamina thickness
$\bar{t}$	=	sheared lamina thickness
T_0	=	fiber angle at beginning of the period with respect to ϕ
T_1	=	fiber angle at middle of the period with respect to ϕ

*PhD Researcher, Bristol Composites Institute, University of Bristol, UK
†Professor in Lightweight Structures, Bristol Composites Institute, University of Bristol, UK and Bernal Chair of Composite Materials and Structures, School of Engineering, University of Limerick, Castletroy, Ireland
‡Senior Lecturer in Composite Structures, Bristol Composites Institute, University of Bristol, UK
§Royal Academy of Engineering Research Fellow, Bristol Composites Institute, University of Bristol, UK

ζ_{kl} = imperfection magnitude Fourier coefficient
θ = total angle sheared
ρ = density of material
ϕ = angle of fiber path with respect to global x-axis
ϕ_{kl} = phase-shift Fourier coefficient

Subscripts

CTS = Continuous Tow Sheared
ex = experimental
imp = imperfect
kl = axial and circumferential wave numbers, respectively
p = perfect
QI = Quasi-isotropic

Superscripts

a, b, c, d, e, m = imperfection signature a, b, c, d, e, m, respectively
k = layer number
μ = mean value
σ = standard deviation

Special symbols

$\sim$ = mass-specific property

II. Introduction

Thin-walled composite cylinders are highly efficient load-bearing structures that offer weight and financial savings when compared to current generation Li-Al fuel tanks [1]. Recent thin-walled shell research has often focused on blade-stiffened shell architectures or skin-and-core sandwich structures [2, 3]. Unstiffened shells are less frequently used owing to their sensitivity to imperfections in compression buckling, the prevailing static load case of launch vehicles. The imperfection sensitivity of thin-walled shells undergoing buckling is well documented. Koiter [4] established that geometric imperfections are the primary imperfection influencing the knockdown of buckling loads, compared to loading or boundary condition imperfections.

Knockdown factors (KDFs), a ratio of experimental buckling load to theoretical buckling load, are often used to describe the imperfection sensitivity of shells quantitatively. Typical results for composite cylinders are exemplified in Fig. 1. Also plotted on Fig. 1 is the 'lower-bound' outlined by the SP-8007 NASA guidelines [6] that was derived from comparing theoretical predictions of buckling loads against experimental results on isotropic cylinders. The relationship is defined as

$$\frac{P_{\text{ex}}}{P_{\text{cl}}} = 1 - 0.901\left(1 - e^{-\Gamma}\right) \qquad \text{for} \qquad \frac{r}{t} < 1500, \tag{1}$$

where Γ is given by

$$\Gamma = \frac{1}{16}\sqrt{\frac{r}{t}}, \tag{2}$$

r is the radius of the cylinder, and t is the wall thickness. For composite cylinders, de Vries [7] suggested a modified formula that used an effective (stiffness-weighted) thickness, t_{eff}, defined as

$$t_{\text{eff}} = \sqrt[4]{\frac{144 D_{11} D_{22}}{A_{11} A_{22}}}, \tag{3}$$

where D_{11}, D_{22}, A_{11}, A_{22} are the bending and in-plane stiffness terms for the laminate. Despite modifications to this guideline, application of legacy KDFs proved too conservative for composite cylinders and lead to over designed structures and unnecessary cost [8].

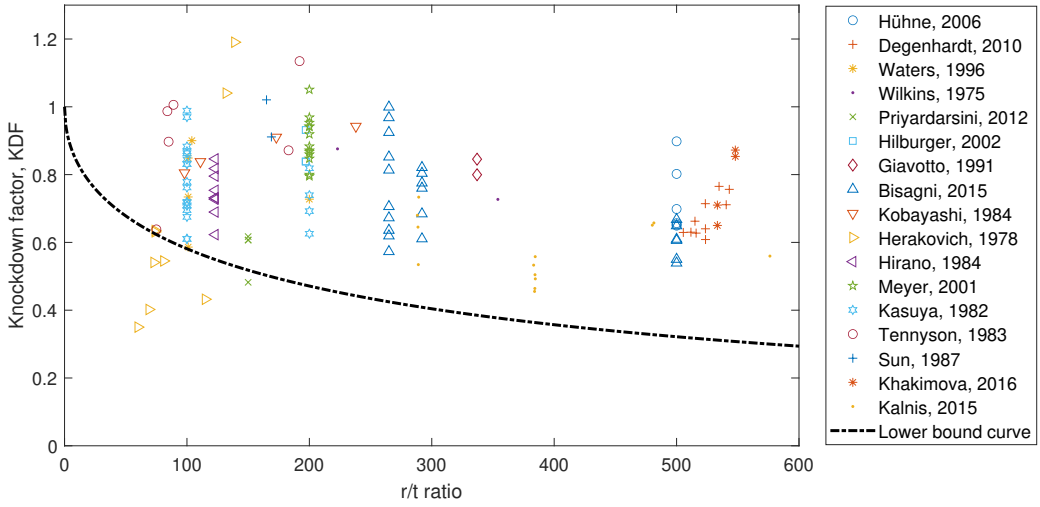

Fig. 1 Composite cylinder data showing the variation in KDF (P_{ex}/P_{cl}) as a function of r/t. Reproduced from [5].

To move away from guidelines that have been shown to be too conservative for composite cylinder, new KDFs have been proposed. These KDFs typically are deterministic or probabilistic. Deterministic KDFs such as those produced by the Reduced Stiffness Method [9], Localised Reduced Stiffness Method [10], Single Boundary Perturbation Approach, Single Perturbation Displacement Approach and Single Perturbation Load Approach [11], and Worse Multiple Perturbation Load Approach [12] have all been developed to account for the differences in theory and experiments. Probabilistic methods were initially proposed by Bolotin [13] due to the irregular imperfections within manufactured shells. Monte Carlo simulations [14] are commonly used to create reliability functions of the buckling load with respect to manufacturing tolerances, material variability and historic imperfections. However, the computational cost of Monte Carlo simulations have lead many researchers to implement the First-Order Second-Moment (FOSM) method that uses a first-order Taylor series to approximate the objective function linearized at the mean values of chosen random variables [15].

Whilst the implementation of new KDFs has led to less conservative designs, limited research has been carried out into removing or minimizing the imperfection sensitivity of axially-compressed monocoque cylinders from a holistic design perspective. Analytical work by Mang et al. [16] and Schranz et al. [17] has shown that the transition from an imperfection-sensitive structure to an imperfection-insensitive one is possible through the use of a stiffening spring attached to the structure. The authors also elucidated that the post-buckling path of such a structure can be influenced by the "load coefficients associated with the secondary (post-buckling) path" [16].

A class of manufacturing techniques have been shown to offer the opportunity to eliminate the need to rely heavily on empirical or computational knockdown factor design guidelines by creating a cylinder that is inherently imperfection *insensitive*. This manufacturing technique creates composite parts that are known as Variable Angle Tow (VAT) composites, which steer fiber-reinforced tapes in curvilinear paths rather than straight trajectories. VAT composites enable tailoring of load paths across a structure which can reduce the likelihood of instabilities initiating. For example, VAT composites documented to increase the mechanical performance of composite plates without a weight penalty [18–21]. White and Weaver [22] have shown that variable-stiffness laminates improve the post-buckling stability of curved shells. Additionally, investigations into the imperfection sensitivity of these shells showed that "perturbing the un-deformed mesh with a component of the linear buckling mode (using a range of positive and negative scaling factors) did not result in an unstable equilibrium path" [22].

The most prevalent VAT manufacturing method is currently Automated Fiber Placement (AFP). Wu et al. [23, 24] have shown that using AFP with large steering radii to create VAT composite cylinders reduces the sensitivity to geometric imperfections by a large margin—KDFs were on average of 0.99 (comparing linear finite element analysis and experimental results). However, process-induced defects are commonplace due to the in-plane bending of tows as the AFP head moves along the curved tow path. The distance of each fiber trajectory from the reference path is different,

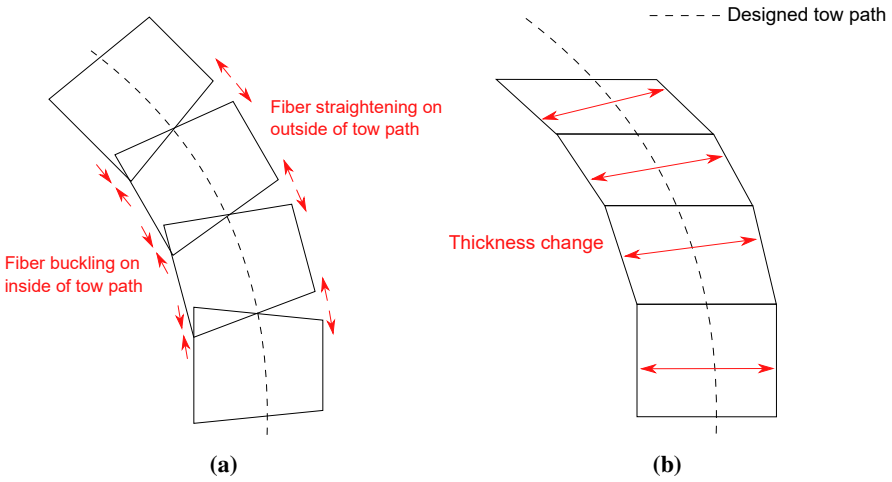

Fig. 2 AFP and CTS tow placement schematic where (a) is AFP and (b) is CTS. Reproduced from Ref. [26].

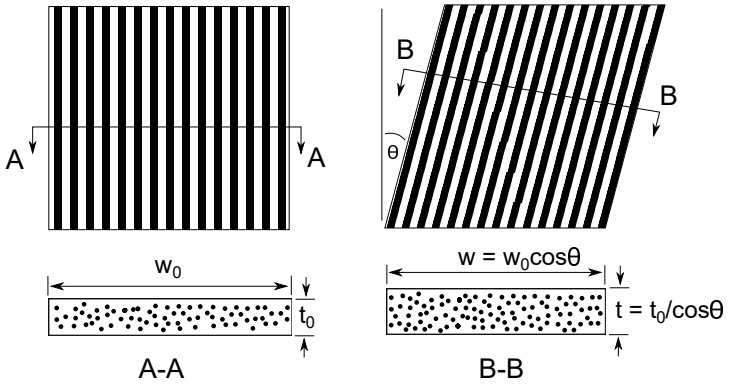

Fig. 3 CTS tow being sheared through a shearing angle θ. Reproduced from Ref. [26].

causing fiber buckling on the inside of the tow and fiber straightening on the outside of the tow [25]. Furthermore, tessellation of laid tows is not possible, leading to either tow gaps or tow overlaps. As a result, the in-plane bending of tows intrinsically limits the steering radius prior to any process-induced defects occurring. Fiber wrinkling, tow gaps and discontinuities are common defects that still challenge the use of curvilinear fiber paths created with AFP.

To counter the process-induced defects associated with AFP, Kim et al. [26] developed the Continuous Tow Shearing (CTS) process. The differences in tow placement strategy between traditional AFP and CTS is shown in Fig. 2. AFP heads are restricted to remain perpendicular to the designed tow path, keeping the tow width constant but causing buckling and straightening if the radius of steering curvature is too small.

In contrast, CTS does not constrain the width of the tow and allows the tows to shear in the plane of placement, the head remaining perpendicular to the initial tow trajectory. This key difference allows perfect tessellation of tows instead of introducing gaps and overlaps. Gaps and overlaps play a significant part in the failure of AFP components [27]. By eliminating these common defects, the shearing process offers a considerable advantage over AFP. A by-product of the shearing action is that there is a thickness build-up perpendicular to the fiber path, as shown in Fig. 3.

The thickness build-up relationship is

$$t = \frac{t_0}{\cos(\theta)}, \tag{4}$$

where t is the thickness of the lamina once sheared, t_0 is the nominal lamina thickness and θ is the shearing angle. The practical limit to the shearing angle is set by manufacturing constraints to be 70° [28], but approaching this angle induces imperfections that could be detrimental to the mechanical performance. The thickness build-up in CTS adds another

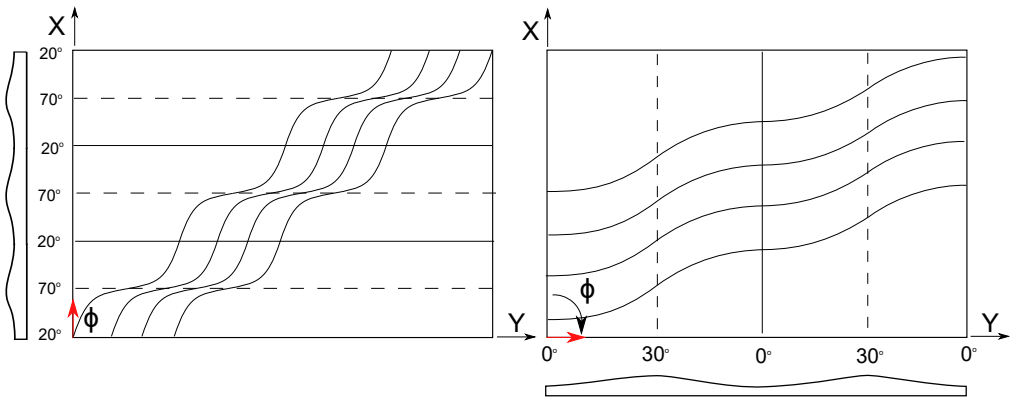

Fig. 4 Single lamina being sheared with the CTS process where the left image is $0\langle 20|70\rangle^3$ and the right image is $90\langle 0|30\rangle^2$.

dimensionality of the design of cylinders, as it opens up the ability to embed hoops, stringers, orthogrids and isogrids within the structure during manufacture. This is not possible with AFP as it does not have the thickness-coupling characteristic of CTS and the steering radius limits the frequency of fiber angle variation.

The present work implements the CTS manufacturing method in three optimizations to maximize specific, imperfect buckling loads. The optimization routines used are Genetic Algorithms (GAs). Each GA incorporates imperfections into an FE model to endeavor to converge on an inherently imperfection insensitive CTS cylinder. The optimization of VAT laminates has shown significant weight-saving capabilities due to the enhanced mechanical properties [29–31], but the seeding of imperfections into the optimization is rare in the literature. Lindgaard et al. [32] optimized straight-fiber cylinders with the "worst" imperfection, taken to be a combination of eigenmodes. This approach gives conservative responses that may not be reflected in the real world; as the authors state "realistic predictions of the collapse load with this method can only be gained with knowledge about the real typical geometric imperfections" [32]. Metamodels [33] are often used in the optimization of multi-variable design problems and have been used to optimize variable-stiffness cylinders [34]. However, the set-up of a metamodel is complex and the issue of imperfection choice still looms. This work attempts to consider both superimposed eigenmode imperfections and realistic composite cylinder imperfections from post-manufacturing measurements in multiple GAs.

The remainder paper is structured as follows. Section III covers the theory and nomenclature of CTS and the parameterization of the three optimizations. The results and discussion of the optimizations are collated in Section IV. Conclusions are summarized in Section V.

III. Theory

A. Continuous Tow Shearing

The fiber-angle convention used herein is similar to that of Gürdal and Olmedo [18] which was used to describe curved fiber paths on a flat plate. As CTS cylinders have a coupling between the fiber angle and thickness, thereby allowing the possibility of embedding stiffeners due to local thickening as the tow is sheared, an additional parameter is needed to define how many times these embedded stiffeners occur. This parameter is termed periodicity and denoted by the letter n. The change in fiber angle is linear across the period. The remaining nomenclature is consistent with that in Ref. [18] so the fiber path is described by

$$\phi\langle T_0|T_1\rangle^n, \tag{5}$$

where ϕ is the clockwise angle from the x-axis that defines the unsheared direction, T_0 is the initial shearing angle measured from ϕ, and T_1 is the shearing angle in the middle of the period. Figure 4 shows the fiber paths that are associated with different ϕ, T_0, T_1 and n values for a single lamina.

It is important to note that the shearing of angled composite ($T_0 \neq 0$) tows within the CTS process is currently untested. For the sake of illustration, a starting angle of $T_0 = 30°$ in a $0\langle 30|50\rangle^1$ ply requires a 'lead-up' from 0° and the

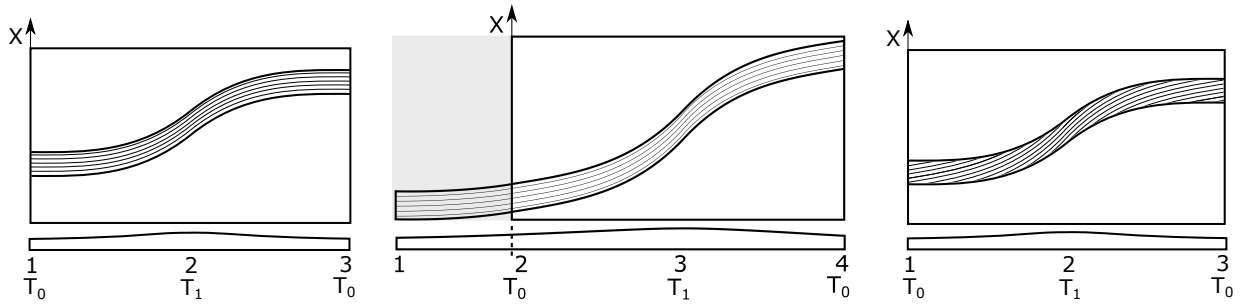

(a) (b) (c)

Fig. 5 Differentiation between current and idealistic manufacturing methods where: (a) is a $90\langle 0|50\rangle^1$ laminate for both methods, (b) is a $90\langle 30|50\rangle^1$ laminate for the current manufacturing method and (c) is shearing $90\langle 30|50\rangle^1$ for the idealistic manufacturing method. For all lamina sheared, the enclosed area is the final ply size. Note the 'preshearing' necessary in Figure 5b to start at 30° where the grey area would be scrap material.

Table 1 Geometry of cylinders, derivative of an Ariane 6 interstage [37] and material properties of respective shells. C1 material is T800/MTM49-3, C2 material is IM7/8552. Both cylinders have 8 plies.

	r [mm]	L [mm]	t [mm]	E_{11} [MPa]	E_{22} [MPa]	ν_{12}	G_{12} [MPa]	G_{13} [MPa]	G_{23} [MPa]	ρ [g/mm^3]
C1	400	1200	1.040	122000	7320	0.31	4900	4900	3230	1.54×10^{-3}
C2	300	1040	1.048	138171	9722	0.356	4900	4900	4900	1.57×10^{-3}

portion of the lamina before 30° would need to be removed before being placed on a mandrel. As previous research [35] has investigated the possible benefits of advancing the manufacturing capabilities to include unsheared angle plies, this is used in optimization 1 of the present work. The shearing of angle plies is herein called the 'idealistic' manufacturing method. The existing manufacturing methodology is herein referred to as the 'current' manufacturing method. Figure 5 shows the differences between the manufacturing methods.

The mass, m, of a CTS cylinder with N layers, radius r, length L and density ρ with current manufacturing ability is

$$m = 2\pi r L \rho \sum_{k=1}^{N} \frac{t^k}{T_1^k - T_0^k} \int_{T_0^k}^{T_1^k} \sec(u)\, du, \tag{6}$$

where t^k, T_0^k and T_1^k, are the nominal thickness, initial shearing angle and final shearing angle (in radians) of the k-th layer, respectively. Interestingly, the periodicity, n, does not appear in this expression, indicating that m is independent of n, a direct measurement of the number of embedded stiffeners. This effect is contrary to typical use of stiffening elements, where more stiffeners leads to an increase in mass.

B. Optimization formulation

The FE solver Abaqus [36] was used to determine the buckling loads of the composite cylinders throughout the optimizations. The material and geometric properties of the cylinders are listed in Table 1. Reduced integration, four-noded elements (S4R) with enhanced hourglassing control were used within the Abaqus environment and a mesh convergence study determined the optimal mesh size [35]. Abaqus *STATIC with NLGEOM=ON was used to calculate the buckling load of cylinders with seeded imperfections by monitoring the FE solver until the first null eigenvalue. The minimum step size was kept relatively large (1×10^{-4}) to converge quickly and offer conservative estimates of buckling loads. Python scripting was utilized to pre-process input files, such as defining element-by-element steered fiber angles, and post-process results, in addition to executing the genetic algorithm.

The three optimizations performed have three distinct aims, and as such, are formulated differently to achieve these aims. Three optimizations are presented as they represent an increasing level of manufacturability, reliability, and computational cost. The first optimization utilizes cylinder C1 from Table 1, the second and third optimizations use

cylinder C2. The change between the two cylinders is related to current manufacturing capabilities. The general layup of the cylinder is constrained to be a balanced, symmetric laminate described by

$$[\phi_1 \pm \langle T_{0_1} | T_{1_1} \rangle^{n_1}, \phi_2 \pm \langle T_{0_2} | T_{1_2} \rangle^{n_2}]_{\mathrm{s}}. \tag{7}$$

For all optimizations the number of elite children was 2, crossover fraction and mutant fraction was 70% and 30% of the remaining population, respectively. These values are similar to literature [22, 31]. For optimization 1 the population size and number of generations was 50. For optimization 2 the population size was 50 and the number of generations 25. For optimization 3 the population size was 30 and the number of generations was 20. The choice of population size and generation number was to keep the simulation time under 7 days for the Abaqus simulations.

1. Optimization 1

The aim of the first optimization was to investigate the possibility of improving the specific buckling load of an imperfect cylinder through an imperfection-seeded optimization. Lincoln et al. [35] performed preliminary investigations into the use of CTS as a mechanism to reduce the imperfection insensitivity of thin-walled, monocoque cylinders and found that, with random geometric imperfections, CTS cylinders can have a specific, imperfect buckling load 8% higher than a QI cylinder. A QI cylinder was used as the benchmark as it is the optimal straight-fiber cylinder layup for axial compression buckling [38]. The preliminary search was not exhaustive however, so a GA was chosen to survey a larger design landscape. Optimizations of fiber angles are known to be non-convex design problems [32] and can produce different solutions depending on the initial conditions. The use of lamination parameters instead of fiber angles transforms the landscape to a convex space [39], but requires a second stage to the optimization to convert the lamination parameters to realistic fiber paths. This two-step process was considered prohibitive at this stage, particularly considering the conversion from lamination parameters to fiber paths for a variable-angle, variable-stiffness, variable-thickness cylinder is a computationally complex task. The optimization is formulated as follows:

$$\begin{aligned}
\max_{x} \quad & \tilde{P}_{\mathrm{imp}}(x) \cdot \min(1, d(x))^3 \\
\text{Variables} \quad & x = [\phi_1, T_{0_1}, T_{1_1}, n_1, \phi_2, T_{0_2}, T_{1_2}, n_2] \\
\text{s.t.} \quad & \phi_i = \{0, 90\} \ (i = 1, 2) \\
& 0 \leq T_{0_i} \leq 90 \ (i = 1, 2) \\
& |T_{1_i} - T_{0_i}| \leq 70 \ (i = 1, 2) \\
& \text{when } \phi_i = 0, \ n_i = 0, 1, 2, ..., 12 \ (i = 1, 2) \\
& \text{when } \phi_i = 90, \ n_i = 0, 1, 2, ..., 25 \ (i = 1, 2) \\
& d(x) = \frac{\tilde{E}_{\mathrm{CTS}}}{0.9 \cdot \tilde{E}_{\mathrm{QI}}}
\end{aligned} \tag{8}$$

where $\tilde{P}_{\mathrm{imp}}$ is the specific, imperfect buckling load of a cylinder and $d(x)$ is an axial stiffness penalty function, reducing the fitness function value if the axial stiffness of the cylinder is less than 90% of that of a QI cylinder. This removes cylinders from the gene pool that have low axial stiffness with a high buckling load—i.e. those that effectively act as axial 'springs'. The exponent 3 was chosen after a trial-and-error study of different integers. The maximum periodicity for $\phi = 0$ and $\phi = 90$ is determined by the minimum shearing radius (taken to be 50 mm [40]) and the length in the direction of ϕ. For $\phi = 90$ the circumferential length is 2513 mm. This caps the maximum number of $T_0 \rightarrow T_1 \rightarrow T_0$ transitions (i.e. periods) to be 25, as the shortest length over which a period can occur is 100 mm. The imperfection used was a superposition of the first twenty eigenmodes of a QI cylinder, each scaled to 1/20$^{\mathrm{th}}$ of a wall thickness.

2. Optimization 2

The aim of optimization 2 was to explore the current manufacturable design landscape and include a computationally inexpensive imperfection robustness test. The cylinder geometry was modified to accommodate physical manufacturing constraints (ply table size and autoclave size). In addition, the current manufacturing constraints do not allow off-axis plies to be sheared, therefore both T_{0_i} and T_{1_i} $(i = 1, 2)$ must be less than 70°. The maximum periodicity has decreased

as the length and circumference of the cylinder have decreased. The optimization is formulated as follows:

$$\begin{aligned}
\max_{x} \quad & \text{mean}\left(\tilde{P}_{\text{imp}}(x)\right) \cdot \min(1, d(x))^3 \\
\text{Variables} \quad & x = [\phi_1, T_{0_1}, T_{1_1}, n_1, \phi_2, T_{0_2}, T_{1_2}, n_2] \\
\text{s.t.} \quad & \phi_i = \{0, 90\} \ (i = 1, 2) \\
& 0 \leq T_{j_i} \leq 70 \ (j = 0, 1, \ i = 1, 2) \\
& \text{when } \phi_i = 0, \ n_i = 0, 1, 2, ..., 10 \ (i = 1, 2) \\
& \text{when } \phi_i = 90, \ n_i = 0, 1, 2, ..., 18 \ (i = 1, 2) \\
& d(x) = \frac{\tilde{E}_{\text{CTS}}}{\tilde{E}_{\text{QI}}}
\end{aligned} \tag{9}$$

where symbols have the same meaning as in Eq. 8. The fitness function evaluation has changed as two imperfections are used throughout the optimization. The mean value of specific imperfect buckling load across these two imperfections is used. The penalty function has increased the threshold for a feasible design so that the axial stiffness must equal that of a QI laminate. The imperfections used were modified to be two different combinations of the first twenty eigenmodes of a QI cylinder. This meant that each cylinder was run through the FE solver twice. After each generation the two imperfections were changed to test the robustness of the elite children and crossover children from the previous generation. The goal of this novel 'dynamic GA' was to mimic an evolutionary process whereby species (CTS cylinders) are continuously being tested by new and changing stressors (imperfections), and the species that survive (remain elite) for the largest set of stressors, are considered to be the best solution. Due to the change in imperfection from generation to generation, the optimization problem is not constant and therefore the GA is not expected to converge. In this sense this exercise is more akin to a guided design landscape exploration.

3. Optimization 3

The aim of the third optimization was to incorporate a well-known probabilistic design tool into the GA to improve the robustness of the GA-optimum cylinder. This optimization is referred to as a 'reliability-based GA' for this reason. To do this, a forward-difference First-Order Second-Moment (FOSM) analysis was used in combination with the GA to evaluate the fitness of a given cylinder. For a full description of the FOSM methodology and implementation, the reader is directed towards References [41–43]. The fundamentals of the approach will be discussed after a description of the imperfections used. To create a more realistic set of imperfections, a repository of Fourier coefficients that describe the imperfections of six manufactured composite cylinders was used [41]. The Fourier coefficients, A_{kl} and B_{kl}, are used to describe a double half wave cosine function

$$z(x, y) = t \sum_{k=0}^{n_1} \sum_{l=0}^{n_2} \cos\left(k\pi \frac{x}{L}\right) \cdot \left(A_{kl} \cos\left(\frac{ly}{r}\right) + B_{kl} \sin\left(\frac{ly}{r}\right)\right), \tag{10}$$

where z is the imperfect cylinder surface of a cylinder of thickness t, length L and radius r. The x and y coordinates are the cylinder length and circumference, respectively. The maximum number of axial, k, and circumferential, l, wave numbers are given by n_1 and n_2, respectively. Kriegesmann et al. [14] suggested using a phase shift approach for composite cylinders as it is more appropriate for probabilistic analyzes. The new formulation of the half wave cosine phase shift is

$$z(x, y) = t \sum_{k=0}^{n_1} \sum_{l=0}^{n_2} \zeta_{kl} \cos\left(k\pi \frac{x}{L}\right) \cdot \cos\left(\frac{ly}{r} - \phi_{kl}\right), \tag{11}$$

where ζ_{kl} and ϕ_{kl} are described by the relationships

$$\zeta_{kl} = \sqrt{A_{kl}^2 + B_{kl}^2}, \tag{12}$$

$$\phi_{kl} = \arctan\left(\frac{B_{kl}}{A_{kl}}\right) \quad \text{for } A_{kl} > 0, \tag{13}$$

$$\phi_{kl} = \arctan\left(\frac{B_{kl}}{A_{kl}}\right) - \pi \quad \text{for } A_{kl} < 0, \tag{14}$$

$$\phi_{kl} = \operatorname{sgn}\left(B_{kl}\right) \cdot \frac{\pi}{2} \quad \text{for } A_{kl} = 0. \tag{15}$$

For the data set considered, n_1 and n_2 are 10 and 20, respectively. This represents $N = (10 + 1) \cdot (20 + 1) \cdot 2 = 462$ different variables to describe the imperfections of a cylinder. These 462 coefficients are the random variables X that are used within the FOSM approach. The buckling load predicted by the FOSM method, $\tilde{P}_{\text{imp}}^{\text{FOSM}}$, which will be the value within the fitness function, is given by

$$\tilde{P}_{\text{imp}}^{\text{FOSM}} = \tilde{P}_{\text{imp}}^{\mu} - b \cdot \tilde{P}_{\text{imp}}^{\sigma}, \tag{16}$$

where $\tilde{P}_{\text{imp}}^{\mu}$ is the buckling load of the mean imperfection signature, b is a factor that defines the chosen reliability limit and assumptions of distribution, and $\tilde{P}_{\text{imp}}^{\sigma}$ is the buckling load of imperfection signature representative of a standard deviation of the imperfection data set. It is assumed the distribution of buckling loads is normal. The calculation of $\tilde{P}_{\text{imp}}^{\sigma}$ is with

$$\tilde{P}_{\text{imp}}^{\sigma} = \sqrt{\text{var}(\tilde{P}_{\text{imp}}(\mathbf{X}))}, \tag{17}$$

where the var is the variance of specific, imperfect buckling loads as a function of the random variables, $\mathbf{X}$. The variance is calculated by

$$\text{var}(\tilde{P}_{\text{imp}}(\mathbf{X})) \approx \sum_{i=1}^{N} \sum_{j=1}^{N} \frac{\partial \tilde{P}_{\text{imp}}}{\partial X_i} \frac{\partial \tilde{P}_{\text{imp}}}{\partial X_j} \text{Cov}(X_i, X_j), \tag{18}$$

where the numerical derivatives $\frac{\partial P}{\partial X_i}$ and $\frac{\partial P}{\partial X_j}$ and the covariance matrix $\text{Cov}(X_i, X_j)$ are to be calculated. Clearly, with $N = 462$ this is computationally expensive. To circumvent this issue the Mahalanobis transformation is used [42] to transform a vector of random variables $\mathbf{X}$ to a vector of uncorrelated variables $\mathbf{z}$ with var of 1 and mean value 0. The transformation is given by

$$\mathbf{X} = \mathbf{Cov}^{\frac{1}{2}}(\mathbf{z} + \boldsymbol{\mu}) \quad \text{and} \quad \mathbf{z} = \mathbf{Cov}^{-\frac{1}{2}}(\mathbf{X} - \boldsymbol{\mu}), \tag{19}$$

where $\boldsymbol{\mu}$ is the mean vector of random variables, $\mathbf{X}$, calculated by

$$\boldsymbol{\mu} = \frac{1}{m} \sum_{k=1}^{N} x_i^k, \tag{20}$$

where m is the number of cylinders in the data set with a unique vector $\mathbf{X}$. In this example, $\mathbf{Cov}$ is rank-deficient as the number of observed cylinders (6) is smaller than the number of random variables (462). Thus, a spectral decomposition is necessary to calculate the root of $\mathbf{Cov}$ described as

$$\mathbf{Cov}^{\frac{1}{2}} = \mathbf{B} = \mathbf{Q}\mathbf{D}^{\frac{1}{2}}, \tag{21}$$

where $\mathbf{Q}$ is the eigenvector matrix of $\mathbf{Cov}$ and $\mathbf{D}$ is the diagonal matrix containing eigenvalues of $\mathbf{Cov}$. Eq. 19 is rewritten to

$$\mathbf{X} = \mathbf{B}(\mathbf{z} + \boldsymbol{\mu}) \quad \text{and} \quad \mathbf{z} = \mathbf{B}(\mathbf{X} - \boldsymbol{\mu}). \tag{22}$$

This reduces the 462 variables needed to describe the distribution of imperfections across six cylinders are reduced to five variables. The variance equation in Eq. 18 can be rewritten to be in terms of the reduced vector $\mathbf{X}$ as

$$\text{var}(\tilde{P}_{\text{imp}}(\mathbf{X})) \approx \sum_{i=1}^{5} \left(\frac{\partial \tilde{P}_{\text{imp}}}{\partial X_i}\right)^2 \text{var}(X_i). \tag{23}$$

As the Mahalanobis transformation assumes the distribution of variables has a variance of 1, $\text{var}(X_i)$ is equal to 1. The numerical derivatives are calculated with a forward difference method, which in the general formulation is

$$\frac{\partial \tilde{P}_{\text{imp}}}{\partial X_i} = \frac{\tilde{P}_{\text{imp}}(X_i + \Delta z_i) - \tilde{P}_{\text{imp}}(X_i)}{\Delta z_i}, \tag{24}$$

Table 2 Reliability % and b factors for a normal distribution.

Reliability %	50	90	99	99.9	99.99	99.999
b	0	1.2815	2.3263	3.0902	3.719	4.2648

where $\tilde{P}_{\text{imp}}(X_i + \Delta z_i)$ is the specific, imperfect buckling load evaluated with the i-th reduced imperfection signature and $\tilde{P}_{\text{imp}}(X_i)$ is the specific, imperfect buckling load evaluated at the mean imperfection signature. The elements of vector $\mathbf{z}$, Δz, are taken to be approximately 1.5, as *var* and standard deviation of the post-Mahalanobis transformation variables is 1. The five imperfections signatures are herein noted by superscript a, b, c, d and e and the mean imperfection signature is denoted by the superscript m. Therefore, the specific, imperfect buckling load with an imperfection signature of a standard deviation of the data set ($\tilde{P}^{\sigma}_{\text{imp}}$) can be rewritten as

$$\tilde{P}^{\sigma}_{\text{imp}} = \left(\left(\frac{\tilde{P}^{a}_{\text{imp}} - \tilde{P}^{m}_{\text{imp}}}{1.5} \right)^2 + \left(\frac{\tilde{P}^{b}_{\text{imp}} - \tilde{P}^{m}_{\text{imp}}}{1.5} \right)^2 + \left(\frac{\tilde{P}^{c}_{\text{imp}} - \tilde{P}^{m}_{\text{imp}}}{1.5} \right)^2 + \left(\frac{\tilde{P}^{d}_{\text{imp}} - \tilde{P}^{m}_{\text{imp}}}{1.5} \right)^2 + \left(\frac{\tilde{P}^{e}_{\text{imp}} - \tilde{P}^{m}_{\text{imp}}}{1.5} \right)^2 \right)^{\frac{1}{2}}. \tag{25}$$

The imperfection signatures that are used to evaluate $\tilde{P}^{a,b,c,d,e}_{\text{imp}}$ are generated with the double wave wave cosine phase shift function with appropriate Fourier coefficients

$$z(x,y)^a = t \sum_{k=0}^{n_1} \sum_{l=0}^{n_2} \zeta^a_{kl} \cos\left(k\pi \frac{x}{L}\right) \cdot \cos\left(\frac{ly}{r} - \phi^a_{kl}\right), \tag{26}$$

where ζ^a_{kl} and ϕ^a_{kl} are the Fourier coefficients after the Mahalanobis transformation in Eq. 22.

The total number of evaluations per CTS laminate is six (one mean, five derivatives). The optimization is formulated as follows:

$$\begin{aligned}
\max_{x} \quad & \tilde{P}^{\text{FOSM}}_{\text{imp}}(x) \cdot \min(1, d(x))^3 \\
\text{Variables} \quad & x = [\phi_1, T_{0_1}, T_{1_1}, n_1, \phi_2, T_{0_2}, T_{1_2}, n_2] \\
\text{s.t.} \quad & \phi_i = \{0, 90\} \ (i = 1, 2) \\
& 0 \leq T_{j_i} \leq 70 \ (j = 0, 1, \ i = 1, 2) \\
& \text{when } \phi_i = 0, \ n_i = 0, 1, 2, ..., 10 \ (i = 1, 2) \\
& \text{when } \phi_i = 90, \ n_i = 0, 1, 2, ..., 18 \ (i = 1, 2) \\
& d(x) = \frac{\tilde{E}_{\text{CTS}}}{\tilde{E}_{\text{QI}}}
\end{aligned} \tag{27}$$

where symbols have their previous meaning. The specific, imperfect buckling load of the FOSM methodology, $\tilde{P}^{\text{FOSM}}_{\text{imp}}$, calculated from Eq. 16 assumes a normal distribution and the reliability factor, b, is set to consider 99.9% of cases. The relationship from reliability % to b factor is shown in Table 2.

IV. Results

The results and discussion of all three optimizations are collated in this section. As each optimization had a specific aim, the post-processing and investigations around the optimum results vary. However, the trends towards imperfection insensitivity by using the CTS manufacturing technique through an optimization with geometrically imperfect thin-walled cylinders shows novel and promising results. These optimizations of thin-walled cylinders with deformations seeded into the geometry are referred to as 'imperfect-geometry' optimizations herein. As the QI cylinder is the optimal composite laminate for thin-walled cylinder buckling, it is used in the present work as the benchmark for the optimizations. The perfect eigenvalue analysis for C1 and C2 cylinder geometries and material systems are collected in Table 3. The key values are the specific, perfect buckling loads, $\tilde{P}_{\text{p}}$. If an imperfect CTS cylinder can approach the perfect behavior of a QI cylinder across a range of imperfections on a mass-specific basis then the uncertainty of designing thin-walled shells decreases, leading to mass and financial savings.

Table 3 Perfect eigenvalue analysis for C1 and C2 geometries and material systems with a QI layup $[\pm 45, 0, 90]_s$.

	P_p [kN]	E_{QI} [GPa]	m [kg]	$\tilde{P}_p$ [kN / kg]	$\tilde{E}_{QI}$ [GPa / kg]
C1	172.0	47.25	4.830	35.61	9.78
C2	198.6	53.26	3.225	61.57	16.51

Table 4 Results from optimization 1 from two runs of the optimization for cylinder C1.

	Layup	m [kg]	$\tilde{P}_{imp}$ [kN / kg]	$\tilde{E}_{CTS}$ [GPa / kg]
GA1.1	$[90 \pm \langle 50\|109\rangle^{22}, 90 \pm \langle 10\|41\rangle^{10}]_s$	5.523	30.00	9.64
GA1.2	$[0 \pm \langle 32\|-12\rangle^{12}, 0 \pm \langle 53\|94\rangle^{11}]_s$	5.347	29.57	9.96

A. Optimization 1

The aim of optimization 1 was to trial the possibility of using an optimization with a built-in imperfection to increase the specific, imperfect buckling and test the robustness of the optimum results. The imperfection used was a superposition of the first 20 eigenmodes of a QI cylinder, all scaled to $1/20^{th}$ of a nominal wall thickness. Cylinders with this imperfections are referred to as 'imperfect$_{QI}$'. The optimization was conducted on cylinder C1. The results from two runs of optimization 1 are collected in Table 4.

The results show that on average, the imperfect$_{QI}$ CTS cylinders have 84% of the buckling load of a perfect (C1) QI cylinder for the same stiffness. To investigate the robustness of the GA-optimum laminates, a comparison of the perfect buckling load, a pseudo-random imperfection signature (referred to as an imperfect$_{Rand}$ cylinder) and the previously used imperfection field (imperfect$_{QI}$) was carried out. Figure 6 plots the end-shortening against the force applied for these three cases.

Interestingly, the imperfect$_{QI}$ cylinder has a higher buckling load than the perfect cylinder. Thus, the use of a single imperfection throughout the optimization resulted in a laminate that has a higher buckling load with an imperfection than without. To investigate this phenomenon further, a brief study into the pre-buckling strain field of the two imperfect cylinders is conducted. The pre-buckling strain field has been shown to have a first-order correlation with the imperfection sensitivity of CTS cylinders [35].

Figure 7 presents the results of this study. Each point on the graph represents an analysis of GA1.1 with the respective imperfection field applied, scaled to the value of imperfection magnitude (x-axis). The buckling load (Fig. 7a) was calculated as described in Section III. The maximum strain difference (Fig. 7b) was calculated by performing a nonlinear step on the imperfect structure up to 0.9 mm (considerably lower than the buckling displacement) and then recording the strain values. This allowed a direct comparison between the pre-buckling strain values of GA1 with QI-derived imperfections and random imperfections.

The buckling load of the imperfect$_{QI}$ GA1.1 does not change as the imperfection magnitude increases to twice the wall thickness. This is a novel result: the GA with a seeded imperfection converges on a laminate that is not influenced by the presence of a large imperfection. The implications of this result is that the random nature of imperfections throughout the manufacturing process could be designed against. It could be possible to include common manufacturing defects in an imperfect-geometry optimization, then the GA can locate a laminate that is inherently insensitive to that imperfection signature. This does not create a *generally* imperfection-insensitive cylinder (a cylinder that is insensitive to many types of imperfections), but the effective removal of imperfection sensitivity for a given imperfection field through a GA is promising. Another approach to removing imperfection sensitivity could be to embed a dominant imperfection during the manufacturing process that is actively designed against. The inclusion of an imperfection to increase the load carrying capacity of a structure is comparable to modal nudging [44], whereby a small geometric change in the stress-free geometry of a structure improves the mechanical performance of the structure. Cox et al. [44] embedded stable, post-buckled deformation modes into the geometry to improve the load carrying capacity of frame structures.

The relationship between buckling load and pre-buckling strain field is found by comparing Fig. 7a and Fig. 7b. As the imperfection magnitude increases for imperfect$_{QI}$ GA1.1 (solid line) the maximum difference between strain

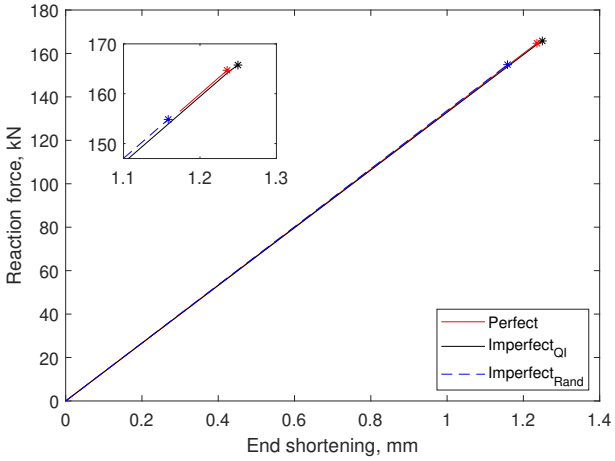

Fig. 6 Reaction force vs. end-shortening plot showing the perfect, imperfect$_{QI}$ and imperfect$_{Rand}$ cylinders.

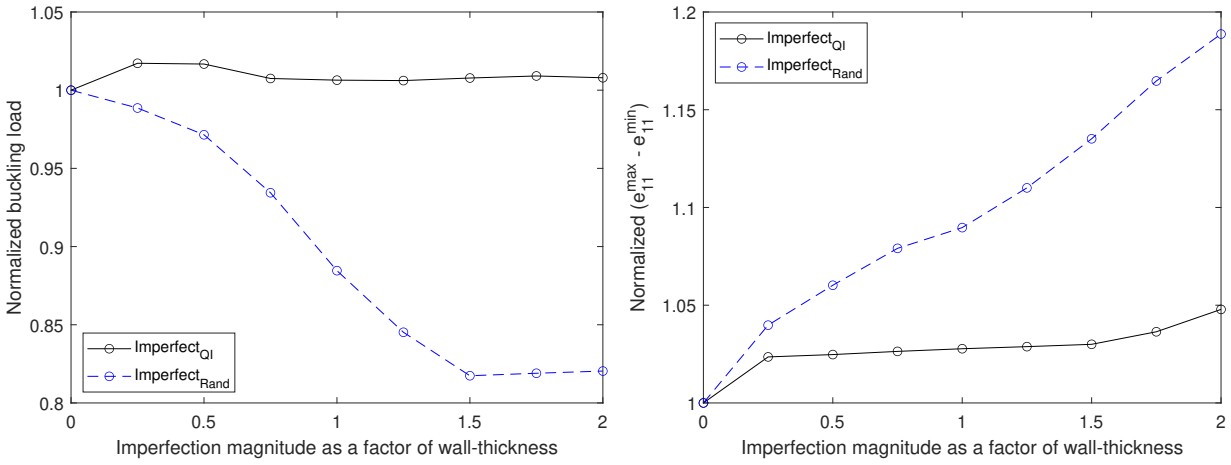

(a) **(b)**

Fig. 7 Relationships between (a) normalized buckling load and imperfection magnitude and (b) normalized maximum strain difference imperfection magnitude for two imperfection signatures, imperfect$_{QI}$ (solid line) and imperfect$_{Rand}$ (dashed line) in the layup GA1.1.

values slowly increases to be 5% larger than the perfect cylinder. This suggests the shearing process has created a non-uniform pre-buckling stiffness field that dominates the pre-buckling response when the QI-derived imperfection field is present. Comparing this trend with the random imperfection signature, the maximum difference between strain values monotonically increases up to 19% more than the perfect cylinder as the imperfection magnitude increases. This reinforces a previous hypothesis that the pre-buckling strain field can be used as an indication of imperfection sensitivity: the more sensitive the pre-buckling strain field is to imperfections, the more sensitive the buckling load is to imperfections [35]. This opens up the possibility of using the pre-buckling strain as a variable to optimize against. The benefit of this approach would be a reduction in computational cost as a small, nonlinear step (*e.g.* to 0.5 mm displacement) is less than a full nonlinear analysis to the bifurcation point.

B. Optimization 2

The aim of optimization 2, based on the results of optimization 1, was to use a dynamic GA that changed the imperfection in each generation with the purpose of finding a cylinder that had a high specific, imperfect buckling load across a range of imperfections. The optimization included the current manufacturing capabilities, a smaller geometry and different material system to enable a manufacturable design. As the imperfection used was variable, the elite

Table 5 CTS cylinders from optimization 2 that had the highest fitness in some generations for cylinder C2.

ID	Layup	m [kg]	$\tilde{P}_{\text{imp}}$ [kN / kg]	$\tilde{E}_{\text{CTS}}$ [GPa / kg]
1	$[0 \pm \langle 20\|25\rangle^2, 90 \pm \langle 35\|25\rangle^9]_s$	3.613	53.22	14.10
2	$[90 \pm \langle 0\|70\rangle^{16}, 0 \pm \langle 15\|0\rangle^3]_s$	3.922	50.13	18.82
3	$[90 \pm \langle 70\|55\rangle^{13}, 0 \pm \langle 10\|15\rangle^5]_s$	5.233	62.22	16.69
4	$[0 \pm \langle 10\|15\rangle^8, 90 \pm \langle 55\|45\rangle^{13}]_s$	4.174	52.55	16.65
5	$[0 \pm \langle 5\|25\rangle^2, 90 \pm \langle 65\|60\rangle^9]_s$	5.181	59.16	15.56
6	$[0 \pm \langle 15\|0\rangle^1, 0 \pm \langle 45\|65\rangle^4]_s$	4.519	50.24	15.14
7	$[90 \pm \langle 70\|25\rangle^{13}, 0 \pm \langle 0\|0\rangle^5]_s$	4.250	52.04	19.53
8	$[0 \pm \langle 0\|5\rangle^{10}, 0 \pm \langle 60\|70\rangle^9]_s$	5.481	53.58	13.09
9	$[90 \pm \langle 60\|35\rangle^{12}, 0 \pm \langle 0\|20\rangle^4]_s$	4.101	49.39	16.90

children (i.e. the laminates with the highest fitness) changed each generation. In addition to changing the imperfection in each generation, two different imperfection signatures were used. The fitness value was evaluated as a mean of the two imperfections. The laminates with high fitness values are shown in Table 5.

General trends from the optimization show that embedded orthogrid structures (CTS laminates that have both $\phi = 0$ and $\phi = 90$) appear to be favorable for imperfection sensitivity. This trend is in line with common industry practice to have hoops and stringers in many thin-walled cylindrical designs. All cylinders listed in Table 5 have 80% of the buckling load of a perfect QI cylinder on a mass-specific basis. One cylinder, Laminate 3, has a higher specific buckling load than a perfect QI cylinder. The optimization results also indicate that when $\phi = 90$, the solver favors higher levels of shearing, resulting in high specific imperfect buckling loads. This is likely due to the embedded stiffeners created in the shearing process when $\phi = 90$. There does not appear to be a trend for placing the embedded stringers/rings on the outside or inside of the laminate. Layers with $\phi = 0$ typically have a lower periodicity (fewer rings) and $\phi = 90$ layers have a higher periodicity (more stiffeners).

There is a general trend to have a highly sheared (T_0 and/or $T_1 > 50$) set of plies within the laminate. This trend alludes to a key trade-off in optimizing for a generally imperfection insensitive cylinder with a high specific imperfect buckling load. As the the specific buckling load is proportional to thickness ($P/m \propto t^2/t \propto t$), increasing the thickness of the cylinder will typically increase the specific buckling load. However, a 'fully sheared' laminate—$T_{0_j} = T_{1_j} = 70$ ($j = 1, 2$)—with a mass of 9.43 kg requires an imperfect buckling load of 725 kN to have a specific, imperfect buckling load that is 80% of the perfect C2 QI cylinder. This laminate architecture would also have no embedded stiffeners, reducing the symmetry-breaking effect of shearing and thereby increasing the imperfection sensitivity.

Laminate 1 was taken forward for a general robustness study and compared against a QI cylinder. Laminate 1 has lower shearing angles when compared to other high fitness designs, but the low shearing angle reduces the likelihood of imperfections during the manufacturing process. As the manufacturing of a CTS cylinder is a novel undertaking, reducing the likelihood of imperfections was considered a priority in selecting a laminate. Laminate 1 from Table 5 is herein referred to as GA2.1.

To test the reliability of the laminate GA2.1 and give an indication to the robustness of the dynamic GA, the buckling load of 1000 geometrically imperfect GA2.1 cylinders was determined. A QI cylinder is also analyzed in the same way for comparison. The geometric imperfections used are pseudo-random imperfections with maximum magnitude of one wall-thickness. Using random geometric imperfections allows for direct comparison between GA2.1 and a QI cylinder as an imperfection signature derived from QI eigenmodes would bias results against the QI cylinder. The same set of 1000 random imperfections are used for GA2.1 and the QI laminate. Figure 8 shows the histogram and overlaid normal probability distributions for GA2.1 and QI cylinders.

Table 6 shows that in all key metrics GA2.1 outperforms the QI cylinder. $\tilde{P}^{\mu}_{\text{imp}}$ for GA2.1 is 1.1% higher than a QI cylinder. GA2.1 demonstrates good reliability characteristics across a range of imperfections, exemplified by the 43% decrease and 81% decrease in standard deviation and variance, respectively.

Comparing the results of this reliability analysis against the dynamic GA, $\tilde{P}^{\mu}_{\text{imp}}$ (from the reliability analysis) is 0.5% higher than $\tilde{P}_{\text{imp}}$ (from the dynamic GA), indicating that the dynamic GA trends towards generally imperfection

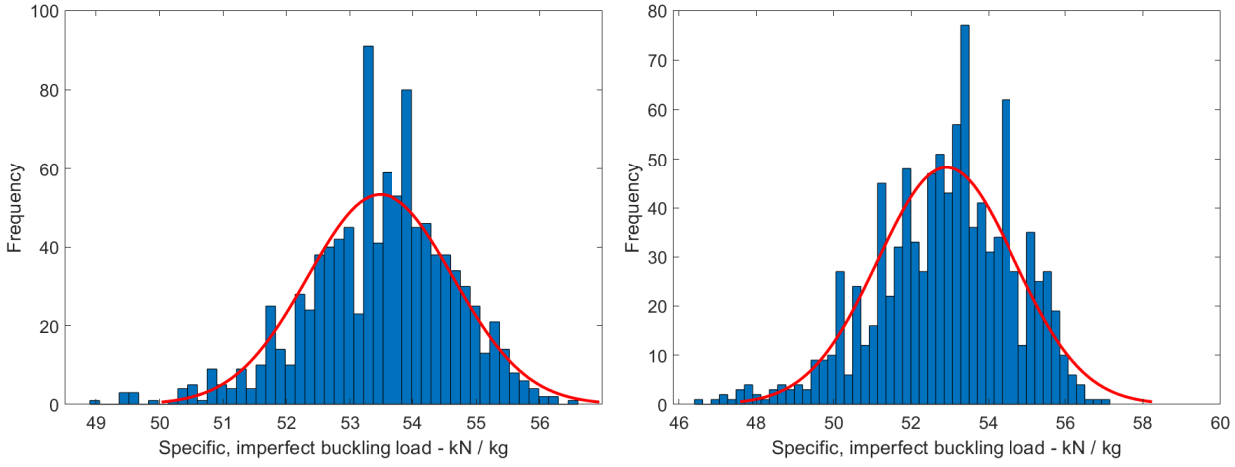

Fig. 8 Histogram and normal probability distribution functions for preliminary reliability test of (a) GA2.1 and (b) QI.

Table 6 Mean, standard deviation and variance of imperfect buckling load, $P_{\mathbf{imp}}$, and specific imperfect buckling load, $\tilde{P}_{\mathbf{imp}}$. Δ% are percentage differences.

	P^{μ}_{imp} [kN]	P^{σ}_{imp} [kN]	var(P_{imp})	$\tilde{P}^{\mu}_{\text{imp}}$ [kN / kg]	$\tilde{P}^{\sigma}_{\text{imp}}$ [kN / kg]	var($\tilde{P}_{\text{imp}}$)
GA2.1	193.4	4.16	84.7	53.5	1.15	0.0234
QI	170.6	5.72	178	52.9	1.78	0.0552
Δ%	+13%	-32%	-71%	+1.1%	-43%	-81%

insensitive cylinders. The Fourier coefficients from a representative pseudo-random imperfection field and randomly selected superimposed QI eigenmodes are presented in Figure 9.

It is clear that the imperfections used have different dominant modes. For the pseudo-random imperfections, $\zeta_{0,2n}$ $(n = 1, 2, 3, ..., 10)$ modes are stronger than most other modes. However, the overall trend shows that many Fourier coefficients have equal weighting. The Fourier coefficients for the first twenty eigenmodes of a QI cylinder are dominated by higher order axial waves. Fourier modes that have ζ values of less than a magnitude 0.005 have been removed from the graph. The Fourier modes shown in Fig. 9 are varied and indicate that GA2.1 is insensitive for different imperfections. However, the Fourier modes exemplified in Fig. 9 are not wholly representative of imperfections seen in the manufacturing of composite cylinders. A more representative set of Fourier coefficients is plotted in Fig. 10.

Figure 10 shows that lower-order Fourier modes are the dominant modes in composite manufacturing. An imperfect-geometry optimization that considers lower-order Fourier modes could lead to a cylinder than is insensitive to these common manufacturing defects.

C. Optimization 3

The purpose of optimization 3 was to incorporate real manufacturing data into a reliability-based GA. Similar to optimization 2, each laminate generated by the GA was evaluated multiple times. As explained in Section III.B.3, there were 6 imperfection signatures (1 mean, 5 derivatives) for each laminate. The target maximum imperfect buckling load, $\tilde{P}^{\text{FOSM}}_{\text{imp}}$, was calculated by Eq. 16. Table 7 presents the results of the optimization against a nominal QI cylinder under the same common manufacturing low-order Fourier modes.

The converged value of the GA has significantly higher $\tilde{P}^{\text{FOSM}}_{\text{imp}}$ values than the QI baseline. Whilst the QI cylinder is not an optimized laminate for the imperfection signature used, it represents a laminate architecture that is commonly used in the design of thin-walled composite cylinders [37]. The significantly higher $\tilde{P}^{\text{FOSM}}_{\text{imp}}$ can be attributed to high mean buckling load and the low standard deviation and variance associated with GA3.1. An imperfection insensitive

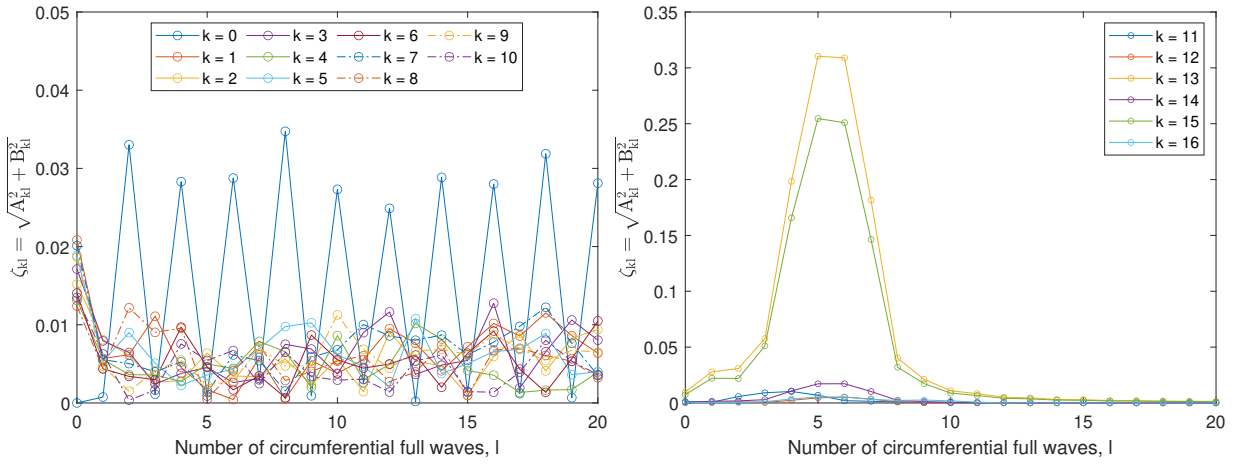

Fig. 9 Fourier modes for (a) pseudo-random imperfection field and (b) random magnitudes of the first twenty eigenmodes of a QI cylinder. All magnitudes of imperfection were scaled up to one wall thickness.

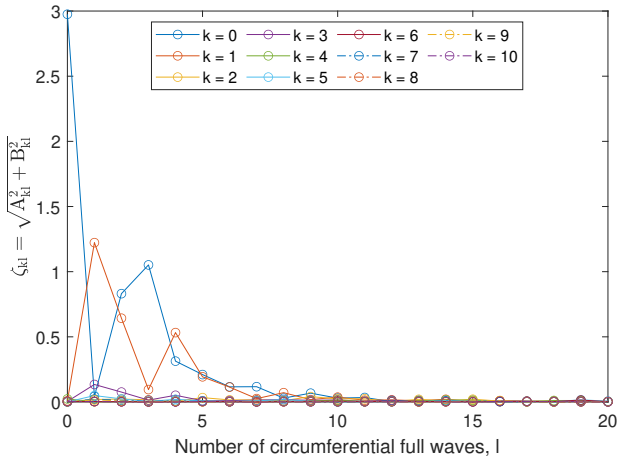

Fig. 10 Example Fourier coefficients for a manufactured composite cylinder, reproduced from [41].

cylinder has been determined through a reliability-based GA optimization. The insensitivity results from the low variance and high reliability load. The KDF, $(\tilde{P}_{\text{imp}}^{\text{FOSM}}/\tilde{P}_{\text{p}})$ of GA3.1 is also higher than the QI baseline, indicating imperfection insensitivity.

GA3.1 has similar characteristics to previous designs in optimization 2: high shearing in $\phi = 90$ plies and a mixture of $\phi = 0$ and $\phi = 90$ plies. The $\phi = 0$ layer has higher periodicity found in optimization 2, possibly due to the GA solver favoring the circumferential stiffening of embedded rings. As the imperfection field is dominated by low-order Fourier modes with $l = 0, 1, ..., 5$ and $k = 0, 1$, the high frequency of rings may act against both the bulging and ovalization modes.

V. Conclusion

In view of the imperfection sensitivity of thin-walled composite cylinders, the CTS manufacturing technique has been employed to reduce said sensitivity through three imperfect-geometry optimizations. The first optimization used a superimposed eigenmode imperfection signature in a GA framework. The results show that the GA-optimum (laminate GA1.1) has a buckling load of 84% of a perfect QI cylinder, the optimal straight-fiber laminate for a cylinder in axial compression buckling [38]. Interestingly, the imperfect$_{\text{QI}}$ GA1.1 (cylinder C1 with $[90 \pm \langle 50|109\rangle^{22}, 90 \pm \langle 10|41\rangle^{10}]_{\text{s}}$

Table 7 Optimization 3 results for GA optimum and QI cylinder for a set of common manufacturing imperfection signatures. $\Delta\%$ are percentage differences.

	Layup	$\tilde{P}^{\text{FOSM}}_{\text{imp}}$ [kN / kg]	$\tilde{P}^{\mu}_{\text{imp}}$ [kN / kg]	$\tilde{P}^{\sigma}_{\text{imp}}$ [kN / kg]	var($\tilde{P}_{\text{imp}}$)	KDF
GA3.1	$[90 \pm \langle 65\|60\rangle^6, 0 \pm \langle 0\|20\rangle^9]_s$	36.9	55.1	5.88	34.6	0.574
QI	$[\pm 45, 0, 90]_s$	9.22	49.7	13.1	171	0.152
$\Delta\%$		+120	+10.3	-76.1	-133	+116

layup seeded with QI eigenmode imperfections) has a higher buckling load when compared to the perfect GA1.1. This holds true for a range of imperfection magnitudes of up to twice the wall thickness of the laminate, showing that the GA solver has converged on a truly imperfection insensitive cylinder (for this specific imperfection) using the CTS manufacturing technique. However, the imperfection insensitivity is specific to the imperfection seeded, as shown in Fig. 6. The results indicate that specific imperfections can be designed against, opening up the possibility of including common manufacturing defects into an imperfect-geometry optimization to produce an imperfection insensitive cylinder.

The second optimization aimed to converge on, through a dynamic GA, a cylinder architecture that was generally imperfection insensitive by combining random magnitudes of superimposed eigenmodes. An optimal cylinder from this optimization had a greater specific, imperfect buckling load than the perfect buckling load of a QI cylinder. A manufacturable design from the dynamic GA was studied with 1000 random geometric imperfections and had a 1.1% higher mean specific, imperfect buckling load and 43% and 81% lower standard deviation and variance, respectively. To further test imperfect-geometry optimizations, a realistic set of manufacturing defects were used in a reliability-based framework in the final optimization. Fourier coefficients were used to describe the imperfection data set and a Mahalanobis transformation was necessary to reduce the number of variables from 462 to 5. The optimization implemented a forward-difference FOSM reliability analysis within the GA to maximize the specific, imperfect buckling load with a reliability threshold of 99.9% assuming a normal distribution. The GA-optimum result shows large improvements over a nominal QI cylinder, increasing the mean specific, imperfect buckling load and reducing the standard deviation and variance.

The variety of imperfections used in the three optimizations show that the CTS manufacturing technique can reduce the imperfection sensitivity of the thin-walled cylinders and GAs are an option for approaching this design problem. However, the choice of imperfection is still key in attempting to reduce imperfection sensitivity. The computational cost of an imperfect-geometry optimization that attempts to include some generality into the solver is an obstacle in finding a generally imperfection insensitive cylinder. Further work to be carried out include a mass-constant buckling optimization of CTS cylinders, both from a perfect geometry and imperfect geometry perspective. Preliminary results in this paper indicate that the CTS manufacturing method holds promise for diminishing the catastrophic influence of imperfections on thin-walled monocoque cylinders.

Acknowledgments

R.L. Lincoln acknowledges the support of the EPSRC [Grant No. EP/L016028/1]. P.M. Weaver acknowledges the support of the Royal Society Wolfson Merit award and the Science Foundation Ireland for the award of a Research Professor grant [Varicomp: 15/RP/2773]. A. Pirrera acknowledges the support of the EPSRC [Grant No. EP/M013170/1]. R.M.J. Groh acknowledges the support of the Royal Academy of Engineering under the Research Fellowship scheme [Grant No. RF/201718/17178]. The underlying data for this publication are available through the University of Bristol data repository.

References

[1] McCarville, D. A., Guzman, J. C., Dillon, A. K., Jackson, J. R., and Birkland, J. O., "Design, manufacture and test of cryotank components," *Comprehensive Composite Materials II*, Vol. 3, 2018, pp. 153–179. https://doi.org/10.1016/B978-0-12-803581-8.09958-6.

[2] National Aeronautics and Space Administration, "Composite Cryotank Technologies and Demonstration," Tech. rep., NASA, 2013.

[3] National Aeronautics and Space Administration, "Shell buckling knockdown factors project," Tech. rep., NASA, 2007.

[4] Koiter, W. T., "A translation of: The Stability of Elastic Equilibrium," Tech. rep., NASA TT-F-10833, 1967.

[5] Wagner, H. N., and Hühne, C., "Robust knockdown factors for the design of cylindrical shells under axial compression: potentials, practial application and reliability analysis," *International Journal of Mechanical Sciences*, Vol. 135, No. November, 2018, pp. 410–430. https://doi.org/10.1016/j.ijmecsci.2017.11.020.

[6] National Aeronautics and Space Administration, "Space Vehicle Design: Buckling Thin-Walled Circular (SP-8007)," Tech. Rep. August, NASA, 1968.

[7] Vries, J. D., "The Imperfection Data Bank and its Applications," Ph.D. thesis, Delft University, 2009.

[8] Hilburger, M. W., "On the development of shell buckling knockdown factors for stiffened metallic launch vehicle cylinders," *AIAA/ASCE/AHS/ASC Structures, Structural Dynamics, and Materials Conference*, Kissimmee, Florida, 2018, pp. 1–17. https://doi.org/10.2514/6.2018-1990.

[9] Croll, J., "Towards Simple Estimates of Shell Buckling Loads." *Der Stahlbau*, Vol. 9, No. 9, 1975, pp. 283–285.

[10] Wagner, H. N., Sosa, E. M., Ludwig, T., Croll, J. G., and Hühne, C., "Robust design of imperfection sensitive thin-walled shells under axial compression, bending or external pressure," *International Journal of Mechanical Sciences*, Vol. 156, No. June 2019, 2019, pp. 205–220. https://doi.org/10.1016/j.ijmecsci.2019.02.047.

[11] Wagner, H. N., Hühne, C., and Niemann, S., "Robust knockdown factors for the design of axially loaded cylindrical and conical composite shells - Development and Validation," *Composite Structures*, Vol. 173, 2017, pp. 281–303. https://doi.org/10.1016/j.compstruct.2017.02.031.

[12] Hao, P., Wang, B., Li, G., Meng, Z., Tian, K., Zeng, D., and Tang, X., "Worst Multiple Perturbation Load Approach of stiffened shells with and without cutouts for improved knockdown factors," *Thin-Walled Structures*, Vol. 82, 2014, pp. 321–330. https://doi.org/10.1016/j.tws.2014.05.004.

[13] Bolotin, V. V., "Statistical Methods in the Nonlinear Theory of Elastic Shells," *Akademii Nauk SSSR, Otdelenie Tekhnicheskykh Nauk [in Russian; English Translation: NASA TTF-85 1962; 1–16].*, Vol. 3, 1958, pp. 33–41.

[14] Kriegesmann, B., Rolfes, R., Hühne, C., Teßmer, J., and Arbocz, J., "Probabilistic design of axially compressed composite cylinders with geometric and loading imperfections," *International Journal of Structural Stability and Dynamics*, Vol. 10, No. 4, 2010, pp. 623–644. https://doi.org/10.1142/S0219455410003658.

[15] Elishakoff, I., Van Manent, S., Vermeulen, P. G., and Arbocz, J., "First-order second-moment analysis of the buckling of shells with random imperfections," *AIAA Journal*, Vol. 25, No. 8, 1987, pp. 1113–1117. https://doi.org/10.2514/3.9751.

[16] Mang, H. A., Schranz, C., and Mackenzie-Helnwein, P., "Conversion from imperfection-sensitive into imperfection-insensitive elastic structures I: Theory," *Computer Methods in Applied Mechanics and Engineering*, Vol. 195, No. 13-16, 2006, pp. 1422–1457. https://doi.org/10.1016/j.cma.2005.05.024.

[17] Schranz, C., Krenn, B., and Mang, H. A., "Conversion from imperfection-sensitive into imperfection-insensitive elastic structures. II: Numerical investigation," *Computer Methods in Applied Mechanics and Engineering*, Vol. 195, No. 13-16, 2006, pp. 1458–1479. https://doi.org/10.1016/j.cma.2005.05.025.

[18] Gurdal, Z., and Olmedo, R., "In-plane response of laminates with spatially varying fiber orientations - Variable stiffness concept," *AIAA Journal*, Vol. 31, No. 4, 1993, pp. 751–758. https://doi.org/10.2514/3.11613.

[19] Raju, G., Wu, Z., Kim, B. C., and Weaver, P. M., "Prebuckling and buckling analysis of variable angle tow plates with general boundary conditions," *Composite Structures*, Vol. 94, No. 9, 2012, pp. 2961–2970. https://doi.org/10.1016/j.compstruct.2012.04.002.

[20] Wu, Z., Weaver, P. M., and Raju, G., "Postbuckling optimisation of variable angle tow composite plates," *Composite Structures*, Vol. 103, 2013, pp. 34–42. https://doi.org/10.1016/j.compstruct.2013.03.004.

[21] Wu, Z., Weaver, P. M., Raju, G., and Chul Kim, B., "Buckling analysis and optimisation of variable angle tow composite plates," *Thin-Walled Structures*, Vol. 60, 2012, pp. 163–172. https://doi.org/10.1016/j.tws.2012.07.008.

[22] White, S. C., and Weaver, P. M., "Towards imperfection insensitive buckling response of shell structures-shells with plate-like post-buckled responses," *The Aeronautical Journal*, Vol. 120, No. 1224, 2016, pp. 233–253. https://doi.org/10.1017/aer.2015.14, URL https://www.cambridge.org/core/product/identifier/S0001924015000147/type/journal_article.

[23] Wu, K. C., Stanford, B. K., Hrinda, G. A., Wang, Z., Martin, R. A., and Kim, H. A., "Structural Assessment of Advanced Tow-Steered Shells," *54th AIAA/ASME/ASCE/AHS/ASC Structures, Structural Dynamics, and Materials Conference*, Boston, Massachusetts, 2013, pp. 1–20. https://doi.org/10.2514/6.2013-1769.

[24] Wu, K. C., Turpin, J. D., Gardner, N. W., Stanford, B., and Martin, R. A., "Structural Characterization of Advanced Composite Tow-Steered Shells with Large Cutouts," *55th AIAA/ASMe/ASCE/AHS/SC Structures, Structural Dynamics, and Materials Conference*, 2014, pp. 1–20. https://doi.org/10.2514/6.2015-0966.

[25] Kim, B. C., Hazra, K., Weaver, P., and Potter, K., "Limitations of fibre placement techniques for variable angle tow composites and their process-induced defects," *18th International Conferences on Composite Materials*, Jeju, Korea, 2011, pp. 1–6.

[26] Kim, B. C., Potter, K., and Weaver, P. M., "Continuous tow shearing for manufacturing variable angle tow composites," *Composites Part A: Applied Science and Manufacturing*, Vol. 43, No. 8, 2012, pp. 1347–1356. https://doi.org/10.1016/j.compositesa.2012.02.024.

[27] Li, X., Hallett, S. R., and Wisnom, M. R., "Modelling the effect of gaps and overlaps in automated fibre placement (AFP)-manufactured laminates," *Science and Engineering of Composite Materials*, Vol. 22, No. 2, 2015, pp. 115–129. https://doi.org/10.1515/secm-2013-0322.

[28] Kim, B. C., Weaver, P. M., and Potter, K., "Manufacturing characteristics of the continuous tow shearing method for manufacturing of variable angle tow composites," *Composites Part A: Applied Science and Manufacturing*, Vol. 61, 2014, pp. 141–151. https://doi.org/10.1016/j.compositesa.2014.02.019.

[29] Wu, Z., Raju, G., and Weaver, P. M., "Optimization of postbuckling behaviour of variable thickness composite panels with variable angle tows: Towards "Buckle-Free" design concept," *International Journal of Solids and Structures*, Vol. 132-133, 2018, pp. 66–79. https://doi.org/10.1016/j.ijsolstr.2017.08.037.

[30] Dodwell, T. J., Butler, R., and Rhead, A. T., "Optimum fiber steering of composite plates for buckling and manufacturability," *AIAA Journal*, Vol. 54, No. 3, 2016, pp. 1139–1142. https://doi.org/10.2514/1.J054297.

[31] Groh, R. M., and Weaver, P., "Mass Optimisation of Variable Angle Tow, Variable Thickness Panels with Static Failure and Buckling Constraints," *56th AIAA/ASCE/AHS/ASC Structures, Structural Dynamics, and Materials Conference*, Kissimmee, Florida, 2015, pp. 1–21. https://doi.org/10.2514/6.2015-0452.

[32] Lindgaard, E., Lund, E., and Rasmussen, K., "Nonlinear buckling optimization of composite structures considering "worst" shape imperfections," *International Journal of Solids and Structures*, Vol. 47, No. 22-23, 2010, pp. 3186–3202. https://doi.org/10.1016/j.ijsolstr.2010.07.020.

[33] Wang, G. G., and Shan, S., "Review of metamodeling techniques in support of engineering design optimization," *Journal of Mechanical Design, Transactions of the ASME*, Vol. 129, No. 4, 2007, pp. 370–380. https://doi.org/10.1115/1.2429697.

[34] Arian Nik, M., Fayazbakhsh, K., Pasini, D., and Lessard, L., "Optimization of variable stiffness composites with embedded defects induced by Automated Fiber Placement," *Composite Structures*, Vol. 107, No. 1, 2014, pp. 160–166. https://doi.org/10.1016/j.compstruct.2013.07.059.

[35] Lincoln, R., Weaver, P., Pirrera, A., and Groh, R., "Imperfection-Insensitive Continuous Tow-Sheared Cylinders," *Composite Structures*, , No. Submitted for Publication, 2019. URL http://hdl.handle.net/1983/192c7097-979b-4413-8daf-fd75b6815909.

[36] Dassult Systèmes, "Abaqus 2018," , 2018. URL https://www.3ds.com/products-services/simulia/products/abaqus/latest-release/.

[37] Wagner, H. N., Petersen, E., Khakimova, R., and Hühne, C., "Buckling analysis of an imperfection-insensitive hybrid composite cylinder under axial compression – numerical simulation, destructive and non-destructive experimental testing," *Composite Structures*, Vol. 225, No. June, 2019, p. 111152. https://doi.org/10.1016/j.compstruct.2019.111152.

[38] Onoda, J., "Optimal laminate configurations of cylindrical shells for axial buckling," *AIAA Journal*, Vol. 23, No. 7, 1985, pp. 1093–1098. https://doi.org/10.2514/3.9042.

[39] Grenestedt, J., and Gudmundson, P., "Layup Optimization of Composite Material Structures," *Optimal Design with Advanced Materials*, edited by P. Pedersen, 1993, pp. 311–336. https://doi.org/10.1016/B978-0-444-89869-2.50027-5.

[40] Zympeloudis, E., Potter, K., Weaver, P. M., and Kim, B. C., "Advanced automated tape laying with fibre steering capability using continuous tow shearing mechanism," *21st International Conferences on Composite Materials*, Xi'an, 2017, pp. 1–6.

[41] Wagner, H., Hühne, C., and Elishakoff, I., "Probabilistic and deterministic lower-bound design benchmarks for cylindrical shells under axial compression," *Thin-Walled Structures*, Vol. 146, No. January, 2020, p. 106451. https://doi.org/10.1016/j.tws.2019.106451.

[42] Kriegesmann, B., Rolfes, R., Hühne, C., and Kling, A., "Fast probabilistic design procedure for axially compressed composite cylinders," *Composite Structures*, Vol. 93, No. 12, 2011, pp. 3140–3149. https://doi.org/10.1016/j.compstruct.2011.06.017.

[43] Schillo, C., Kriegesmann, B., and Krause, D., "Reliability based calibration of safety factors for unstiffened cylindrical composite shells," *Composite Structures*, Vol. 168, No. May, 2017, pp. 798–812. https://doi.org/10.1016/j.compstruct.2017.02.082.

[44] Cox, B. S., Groh, R. M., Avitabile, D., and Pirrera, A., "Modal nudging in nonlinear elasticity: Tailoring the elastic post-buckling behaviour of engineering structures," *Journal of the Mechanics and Physics of Solids*, Vol. 116, 2018, pp. 135–149. https://doi.org/10.1016/j.jmps.2018.03.025, URL https://doi.org/10.1016/j.jmps.2018.03.025.